Journal of Colloid and Interface Science 677 (2025) 997–1004

Contents lists available at ScienceDirect

Journal of Colloid And Interface Science

journal homepage: www.elsevier.com/locate/jcis

Electronic regulation of hcp-Ru by *d-d* orbital coupling for robust electrocatalytic hydrogen oxidation in alkaline electrolytes

Yi Liu [a], Lianrui Cheng [a], Shuqing Zhou [a], Chenggong Niu [a], Tayirjan Taylor Isimjan [b,*], Xiulin Yang [a,*]

[a] Guangxi Key Laboratory of Low Carbon Energy Materials, School of Chemistry and Pharmaceutical Sciences, Guangxi Normal University, Guilin 541004, China
[b] Saudi Arabia Basic Industries Corporation (SABIC) at King Abdullah University of Science and Technology (KAUST), Thuwal 23955-6900, Saudi Arabia

HIGHLIGHTS

- RuCo alloy nanoparticles is fabricated by impregnation and pyrolysis strategies.
- The hollow mesoporous structure facilitates ion diffusion and electron transport.
- The hcp-RuCo@C exhibits good HOR activity and resistance to CO poisoning.
- Alloying-induced *d-d* electronic interaction optimizes the HBE and OHBE, promoting the vital Volmer step.

GRAPHICAL ABSTRACT

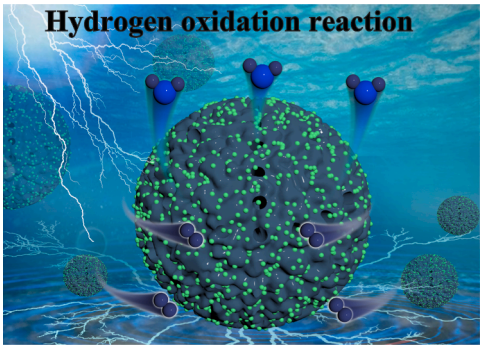

ARTICLE INFO

Keywords:
Bimetallic alloy
Electrocatalysis
d-d electronic interactions
Hydrogen oxidation reaction

ABSTRACT

Bimetallic alloys hold exceptional promise as candidate materials because they offer a diverse parameter space for optimizing electronic structures and catalytic sites. Herein, we fabricate ruthenium-cobalt alloy nanoparticles uniformly dispersed within hollow mesoporous carbon spheres (hcp-RuCo@C) via impregnation and pyrolysis strategies. The intriguing hollow mesopore structure of hcp-RuCo@C facilitates efficient contact between active sites and reactants, thereby accelerating hydrogen oxidation reaction (HOR) kinetics. As anticipated, the hcp-RuCo@C showcases remarkable exchange current density and mass activity of 3.73 mA cm^{-2} and 2.8 mA μg_{Ru}^{-1}, respectively, surpassing those of commercial Pt/C and documented Ru-based electrocatalysts. Notably, hcp-RuCo@C demonstrates robust resistance to 1000 ppm CO, a trait lacking in Pt/C catalysts. Comprehensive experimental results reveal that the alloying-induced *d-d* electronic interactions between Ru and Co species significantly optimizes hydrogen binding energy (HBE) and hydroxide binding energy (OHBE). This optimization promotes the vital Volmer step, ameliorating the alkaline HOR properties of hcp-RuCo@C.

* Corresponding authors.
E-mail addresses: isimjant@sabic.com (T. Taylor Isimjan), xlyang@gxnu.edu.cn (X. Yang).

https://doi.org/10.1016/j.jcis.2024.08.136
Received 13 May 2024; Received in revised form 2 August 2024; Accepted 18 August 2024
Available online 20 August 2024

1. Introduction

Amidst a global consensus on pivotal actions to address climate and environmental concerns, the utilization of hydrogen-centric energy systems is receiving mounting attention [1]. Hydrogen-oxygen fuel cells (HOFC) offer high energy efficiency and durability, paving the way for establishing a sustainable energy infrastructure based on electrical hydrogen generated from renewable resources [2,3]. Recent advancements in non-precious cathodic oxygen reduction reaction (ORR) electrocatalysts and anion-exchange membranes have significantly reduced the cost of fuel cell systems [4,5]. Nevertheless, the widespread adoption of anion-exchange membrane fuel cells (AEMFCs) heavily relies on the efficiency and durability of the HOR electrocatalysts, as the HOR kinetics of platinum-group metals in alkaline environments present significant challenges compared to acidic conditions [6–8]. Despite tremendous progress in developing high-performance HOR electrocatalysts such as alloy materials [9], single-atom catalysts [10], and heterostructure compounds [11], etc., the ongoing goals for practical commercial applications include further reducing the use of precious metals and enhancing electrochemical stability. Therefore, crafting low-cost, efficient and high stability HOR catalysts under operational conditions is pivotal for commercializing AEMFC technology.

The alkaline HOR process involves the dissociation of H_2 to form adsorbed hydrogen (H_{ad}), as well as the combination of H_{ad} and adjacent hydroxyl groups (OH^-) to form water [12,13]. Hydrogen binding energy (HBE) and hydroxyl binding energy (OHBE) are crucial parameters for evaluating alkaline HOR [14,15]. Ruthenium (Ru) possesses similar metal-hydrogen bond strength to platinum (Pt), relatively economical cost, appropriate oxyphilic capacity, and optimal adsorption of OH_{ad} and H_{ad} at low anode potential, which is essential for achieving rapid HOR kinetics in alkaline environments [16,17]. To some extent, Ru-based electrocatalysts are deemed as potential alternatives to Pt. However, as the anodic potential increases, metallic Ru is incapable to maintain an adequate oxide-free surface to bind with H_{ad}, because it is susceptible to oxidation at higher anodic potentials (>0.1 V vs. RHE) [18]. Therefore, there is a need to modulate the electronic structure of Ru to manufacture Ru-based HOR electrocatalysts with exceptional activity and durability. Coupling Ru with *d-d* orbitals of heteroatoms (Fe, Co, and Ni) to manipulate the *d*-band centers relative to the Ru Fermi level can alter the surface structure of Ru, weakening the HBE and enhancing the OHBE, thus boosting the HOR activity of Ru-based catalysts [19,20]. For instance, Yuan et al. utilized the polymer-assisted pyrolysis method to fabricate FeCoNiMoW high-entropy alloy (HEA) nanoparticles embedded within a porous carbon skeleton, which exhibited remarkable activity and durability in an alkaline environment [21]. Moreover, innovating open nanostructures, such as hollow mesoporous spheres, proven effective in amplifying the electrocatalytic peculiarity of alloy materials, expediting efficient reactant mass transfer across outer and inner surfaces and creating more active sites [22].

In this study, we synthesized bimetallic RuCo nanoalloy using a wet-chemical-pyrolysis strategy, and evaluated its catalytic performance for HOR under alkaline condition. Benefiting from the unique hollow mesoporous structure and alloying effect, hcp-RuCo@C exhibited a larger specific surface area, decreasing diffusion resistance and providing a high density of active sites. Consequently, hcp-RuCo@C demonstrated a synergistic combination of high activity, decent durability, as well as superb CO tolerance, showcasing its potential application in energy conversion devices. Experimental results disclosed that the *d-d* electronic interactions between Ru and Co optimized the adsorption of both hydrogen and hydroxyl species, which significantly advances the crucial Volmer step.

2. Experimental section

2.1. Chemicals and reagents

All materials were employed without any further purification. These included tetraethyl silicate (TEOS), ammonia solution (NH_4OH), 3-hydroxytyramine hydrochloride ($C_8H_{11}NO_2{\cdot}HCl$), ruthenium trichloride ($RuCl_3{\cdot}xH_2O$, 99 %, ~40 wt.% Ru), cobaltous acetate ($C_4H_6CoO_4$, 99.5 %), trimesic acid (H_3BTC, 99 %), methanol absolute (CH_3OH, 99.5 %), commercial Pt/C (20 wt% Pt), nafion solution (5 wt %), and potassium hydroxide (KOH, 90.0 %).

2.2. Synthesis of hollow mesoporous carbon spheres (HMCS)

The hollow mesoporous carbon spheres were synthesized according to our previous work [23].

2.3. Synthesis of hcp-RuCo@C nanoalloy, hcp-Ru@C, and Co@C

The typical synthesis of hcp-RuCo@C catalyst was as follows. Briefly, a specific amount of HMCS support was dispersed in 40 mL of mixed solution (deionized water/methanol absolute: = 1/1 *v/v*) containing 20 mg ruthenium trichloride, 30 mg cobaltous acetate and 20 mg trimesic acid. Followed by an oil bath for 12 h at 60 °C. The precursor was harvested by centrifugation, washed with water and ethanol for several times, and dried in a vacuum oven overnight. Subsequently, the precursor was then pyrolysed at 500 °C for 2 h at a heating rate of 5 °C min^{-1} in an N_2 atmosphere. After naturally cooling, the obtained sample was denoted as hcp-RuCo@C, with a specific Ru content of 4.68 wt.%, affirmed by inductively coupled plasma (ICP-MS) measurements.

As a control, the preparation of hcp-Ru@C, and Co@C was similar to that of hcp-RuCo@C, in the absence of ruthenium trichloride (cobaltous acetate).

2.4. Materials characterization

The samples' crystal structure and phase composition of the samples were examined using Powder X-ray diffraction (XRD) with a Rigaku D/Max 2500 V/PC instrument, which utilized Cu Kα radiation to scan the 2θ range from 10 to 90 degrees. The morphology and elemental distribution of the catalysts were characterized through scanning electron microscopy (SEM, FEI Quanta 200 FEG) and transmission electron microscopy (TEM, JEM-2100F). X-ray photoelectron spectroscopy (XPS) with a JPS-9010 instrument utilizing Mg Kα radiation analyzed the samples' chemical state and electronic structure. The metal content in the catalysts was determined using inductively coupled plasma mass spectroscopy (ICP-MS, PerkinElmer corporation, FLexar-NexION300X). The samples' specific BET surface area (Brunauer–Emmett–Teller) and pore size distribution were used to measure the specific surface area and pore size distribution, respectively. Raman spectra were recorded using a Renishaw in Via instrument with a visible laser set at 532 nm.

2.5. Electrochemical measurements

The CHI 760E (Shanghai, China) electrochemical analyzer was used to perform all the electrochemical measurements in a standard three-electrode system. A glassy carbon electrode (GCE, diameter: 5 mm, disk area: 0.196 cm^2) coated with catalysts acted as the working electrode. The Ag/AgCl electrode (in 0.1 M KOH) and the graphite rod were the reference electrode and counter electrode, respectively. All measured potentials were reported versus the reversible hydrogen electrode (RHE) potential.

2.6. Preparation of catalytic electrodes

To fabricate a thin-film working electrode, 3 mg of sample and 5 μL

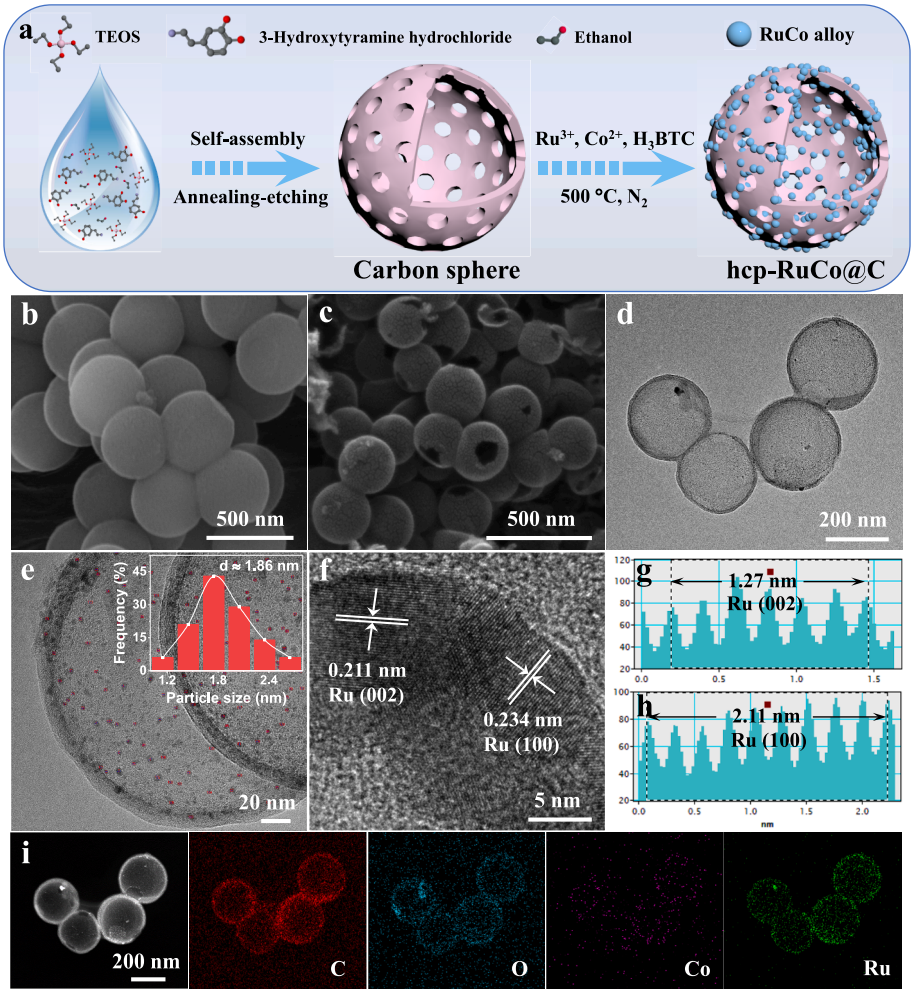

Fig. 1. (a) Schematic illustration of the fabrication of hcp-RuCo@C. SEM images of (b) SiO_2@DA and (c) hcp-RuCo@C. (d–e) TEM images and corresponding particle size statistics of hcp-RuCo@C. (f–h) High-resolution TEM image and lattice analysis. (i) HAADF-STEM and corresponding elemental mappings of hcp-RuCo@C.

of Nafion solution (5 wt.%), were ultrasonically dispersed in deionized water-isopropanol solution (volume ratio,1: 1) to form a homogeneous ink. Then, 10 μL ink was pipetted onto the surface of a pre-polished glassy carbon electrode, drying the ink before measurement. The amount of Ru loading was 14.29 μg_{Ru} cm^{-2}, calculated by ICP-MS data (Table S1).

2.7. Hydrogen oxidation reaction (HOR) measurements

Cyclic voltammetry (CV) curves were recorded between 0 V and 1.0 V vs. reversible hydrogen electrode (vs. RHE) in a pre-made N_2-saturated 0.1 M KOH electrolyte until stable curves were obtained. The HOR polarization curves were recorded by a rotation disk electrode (RDE) with a rotation speed of 1600 rpm in an H_2-saturated 0.1 M KOH, and the potential range is from −0.05 V to 0.5 V at a scanning rate of 10 mV s^{-1}.

The HOR polarization under the rotation speed of 2500, 1600, 900, and 400 rpm were collected at a scanning rate of 10 mV s^{-1}. The kinetic current density (j_k) of each electrocatalyst could be calculated from the Koutecky-Levich equation (Eq. (1)):

$$\frac{1}{j_d}+\frac{1}{j_k}=\frac{1}{j} \tag{1}$$

Where j_d is the diffusion current density [mA cm^{-2}], j_k is the kinetic current density [mA cm^{-2}], and j is the measured current density [mA cm^{-2}].

Levich equation (Eq. (2)):

$$j_d = 0.62nFD^{3/2}\nu^{-1/6}C_0\omega^{1/2} = BC_0\omega^{1/2} \tag{2}$$

In the formula, n, F, and D correspond to the number of electrons transferred in the HOR, the Faraday constant (96485 C mol^{-1}), and H_2 diffusivity in the electrolytes (3.7×10^{-5} cm^2 s^{-1}), respectively. B is the Levich constant, C_0 is the solubility of H_2 (7.33×10^{-4} mol L^{-1}) and ω is the rotating speed.

Exchange current density (j_0) could be deduced from the Butler–Volmer equation in Eq. (3):

$$j_k = j_0\left[e^{\eta\frac{\alpha F}{RT}} - e^{\eta\frac{-(1-\alpha)F}{RT}}\right] \tag{3}$$

where η, α is the overpotential and transfer coefficient, R and T represent the gas constant (8.314 J mol^{-1} K^{-1}) and the testing temperature (303 K), respectively.

Mass activity (MA) was normalized by using j_k and the mass active metal dripped onto the RDE (Eq. (4).

$$MA = \frac{j_k}{M} \tag{4}$$

CO stripping voltammetry measurements was performed by holding the potential of working electrode at 0.1 V (vs. RHE) for 10 min in the UHP CO to adsorb CO on the metal surface fully. Following, N_2 was bubbled for 40 min to remove residual CO in the electrolyte completely. CO

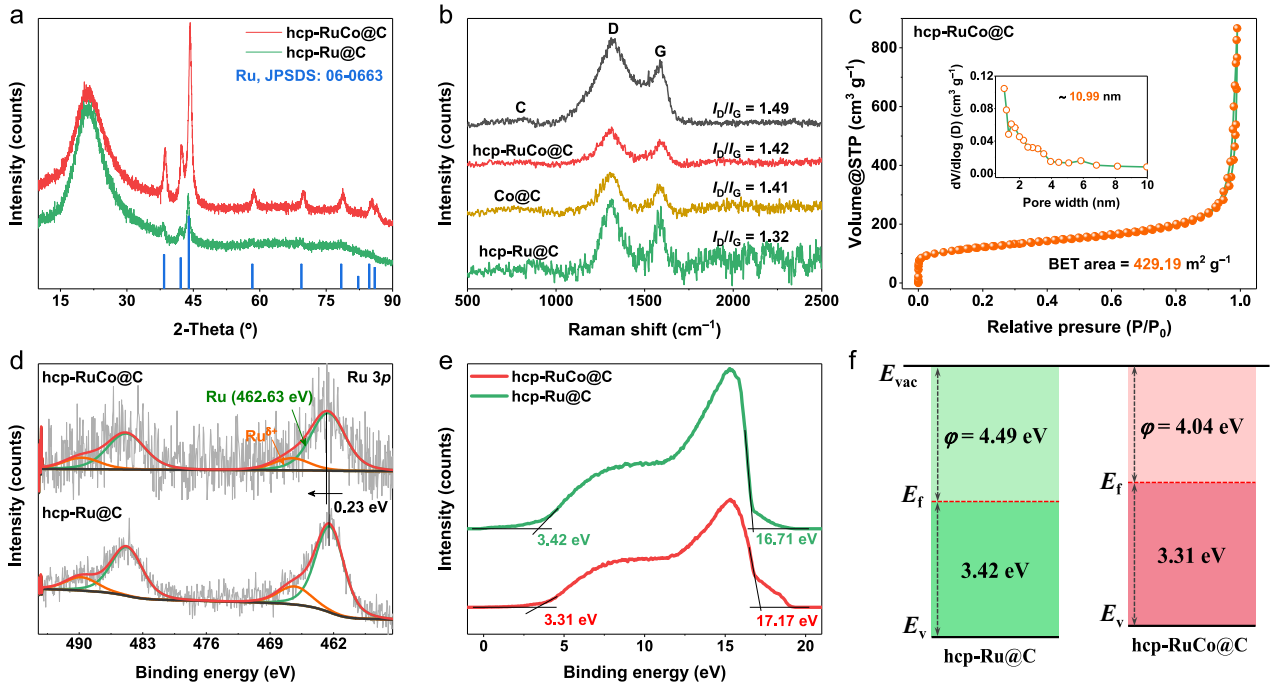

Fig. 2. (a) XRD patterns of hcp-RuCo@C and hcp-Ru@C. (b) Raman spectra of hcp-RuCo@C, hcp-Ru@C, Co@C and C. (c) N_2 adsorption–desorption isotherms and pore size distribution (inset) of hcp-RuCo@C. (d) High resolution XPS of Ru 3*p* in hcp-RuCo@C and hcp-Ru@C. (e) UPS spectra and (f) band structure alignment of hcp-RuCo@C and hcp-Ru@C.

stripping current was obtained by cycling between 0 V and 1.2 V (vs. RHE) at 0.02 V s^{-1} without any extra CO. The 1st CV is the stripping of the monolayer CO, where the CO oxidation peak can be noticed. The 2nd CV represented the background (Eq. (5).

$$ECSA_{active\ metal} = \frac{Q_{co}}{0.42\ mC\ cm^{-2} * M} \quad (5)$$

where Q_{CO} is the total charge of adsorbed CO oxidation, 0.42 mC cm^{-2} corresponds to monolayer CO adsorption, and M represents the total loading of active metal on the working electrode.

3. Results and discussion

3.1. Synthesis and structural analysis

Fig. 1a illustrated the overall synthetic pathway for hcp-RuCo@C, involving impregnation and carbonization strategies. Briefly, SiO_2@DA (DA: dopamine) was initially synthesized using a one-pot approach. Hollow mesoporous carbon spheres (HMCS) were obtained after carbonization and desilication. Subsequently, HMCS were dispersed ultrasonically in a mixed aqueous solution containing Ru salt, Co salt, and H_3BTC, resulting in the formation of hcp-RuCo@C through annealing at 500 °C in N_2 atmosphere. For comparison, the hcp-Ru@C catalyst was prepared by a similar process. The morphological evolution of HMCS and hcp-RuCo@C were investigated using SEM characteristic. As depicted in Fig. 1b, SiO_2@DA appeared a monodispersed spherical morphology. After pyrolysis and alkali-steeping, the initial solid sphere transformed into a hollow spherical shape (Fig. S1). Notably, hcp-RuCo@C retained the distinctive hollow spherical morphology inherited from HMCS (Fig. 1c). The hollow spherical structure afforded a superiority in erasing the inert interior blockage and curtailing the distance for reactant transport compared to an intact sphere [24,25]. Transmission electron microscopy (TEM) images (Fig. 1d) verified the hollow spherical nature of hcp-RuCo@C. Profiting from the synergistic effect between Co and Ru species, RuCo nanoparticles were evenly distributed throughout the hollow spherical structure, resulting in a small average particle size of 1.86 nm (Fig. 1e). In contrast, pure hcp-Ru@C (4.16 nm) tended to aggregate on the support. This led to a distinctly larger nanoparticle size on the carrier surface and covered many active sites, which contributed to poor catalytic performance (Fig. S2a). High-resolution TEM (HR-TEM) analysis (Fig. 1f-h) indicated lattice streak spacing of 0.211 and 0.234 nm aligning with the (0 0 2) and (1 0 0) crystal facets of hcp-Ru, respectively. Compared with hcp-Ru@C (Fig. S2b), the crystal plane spacings of hcp-RuCo@C exhibited a certain reduction, validating the successful incorporation of Co atom into the Ru lattices [26]. Elemental mapping analysis further confirmed the homogeneous spatial distributions of C, O, Co and Ru elements within the structure (Fig. 1i).

X-ray diffraction (XRD) analysis (Fig. 2a) revealed that both hcp-RuCo@C and hcp-Ru/C exhibited a well-matched hexagonal-close-packed (hcp) structure (JCPDS: 06–0663) [27]. Remarkably, the XRD peaks around 44° for hcp-RuCo@C shifted positively to higher angle than hcp-Ru@C, indicating the smooth incorporation of Co atoms into the Ru lattice. Raman spectroscopy was then employed to assess the structural defects of the samples. Fig. 2b showed that the intensity ratio (I_D/I_G) between D (≈ 1319 cm^{-1}, disordered/defective C-sp^3) and G (≈ 1581 cm^{-1}, ordered graphitic C-sp^2) bands for the HMCS support was approximately 1.49, suggesting the richness of structural defects in the carbon carriers [28]. Whereas the I_D/I_G ratio of hcp-RuCo@C was slightly lessened, likely due to the occupation of some carbon defective sites by RuCo alloy nanoparticles. This suggested that HMCS can be a protective shell, preventing RuCo alloy nanoparticles' agglomeration, exfoliation, and dissolution during electrochemical measurements, thus upholding their prolonged stability [25,29]. As showed in Fig. 2c, the specific surface area of hcp-RuCo@C determined by Brunauer–Emmett–Teller (BET) was about 429.19 m^2 g^{-1}, and possessed abundant pore structure (average pore size ≈ 10.99 nm), which was conducive to H_2 adsorption and electron/mass transport on catalyst surface, thus enhancing its catalytic performance [23,30].

Moreover, the variation of surface chemical states after alloying with Co was thoroughly appraised by X-ray photoelectron spectroscopy (XPS). In the high-resolution Ru 3*p* spectra (Fig. 2d), the deconvoluted

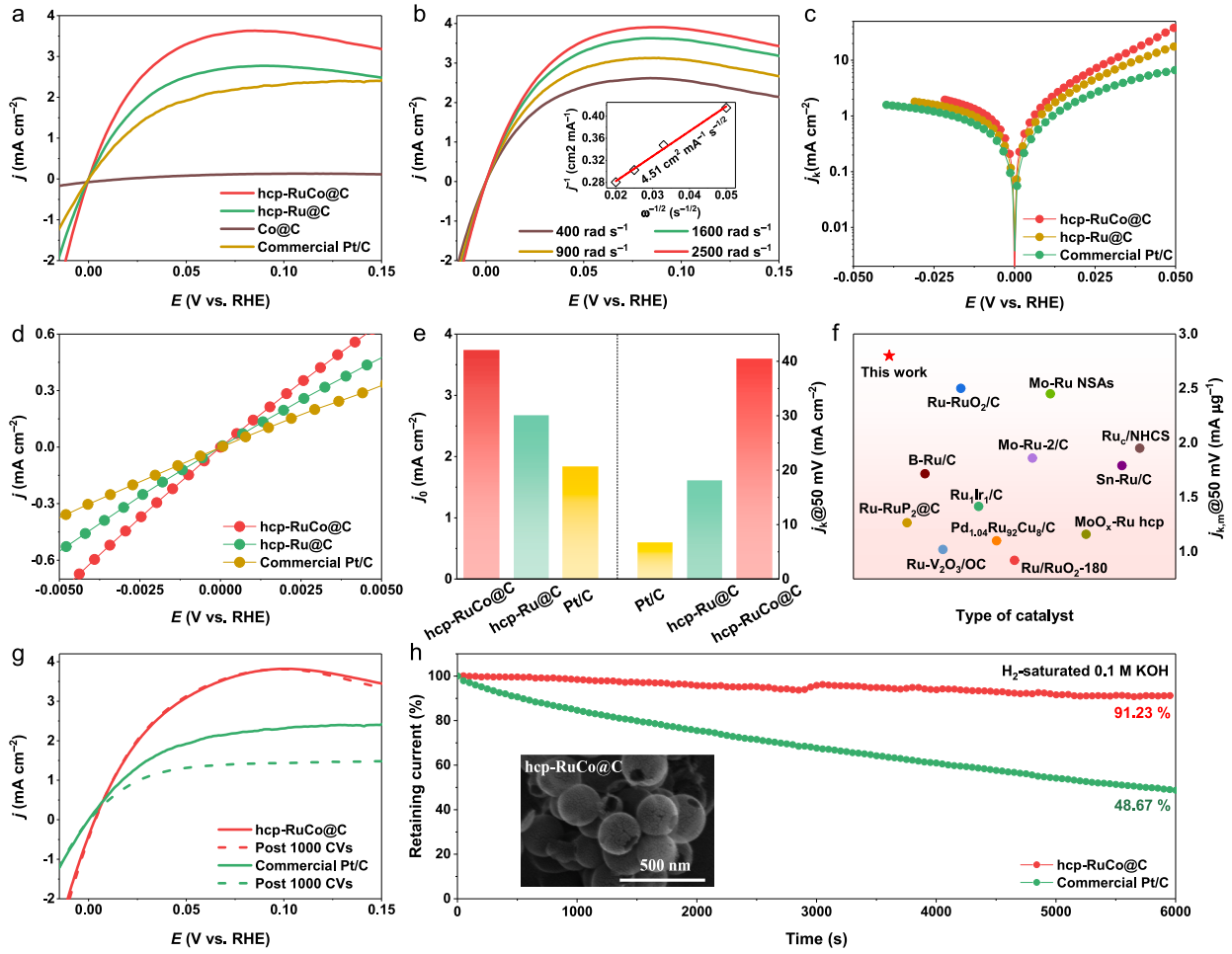

Fig. 3. (a) HOR polarization curves of hcp-RuCo@C, hcp-Ru@C, Co@C and commercial Pt/C, respectively. (b) HOR polarization curves for hcp-RuCo@C at various rotation speeds. Inset in b shows corresponding Koutecky-Levich plots at 50 mV. (c) Tafel plots. (d) Linear fitting curves in micropolarization region. (e) Comparison of j_k and j_0 of studied electrocatalysts. (f) Compared the MA with other recently reported alkaline HOR electrocatalysts. (g) HOR polarization curves for hcp-RuCo@C and commercial Pt/C in H_2-saturated 0.1 M KOH before and after 1000 cycles. (h) Chronoamperometry (*j-t*) responses were recorded on hcp-RuCo@C and commercial Pt/C. The inset shows the SEM image of hcp-RuCo@C after long-term stability.

peaks at 462.63 and 484.86 eV corresponded to bulk metallic Ru, while the peaks centered at 466.60 and 489.72 eV accounted for electro-depleted ruthenium species ($Ru^{\delta+}$). Apparently, the metallic Ru peak of hcp-RuCo@C emerged a positive shift of 0.23 eV in contrast to pure hcp-Ru@C, which explained the electron transfer from Ru to Co, inducing a violent *d-d* electron interaction, which was conducive to enhancing HOR activity [31]. Additionally, the electronic characteristics of hcp-RuCo@C were thoroughly investigated using ultraviolet photoelectron spectroscopy (UPS) to delve into its augmented intrinsic activity and rapid reaction dynamics. Fig. 2e-f revealed that the work function (WF) values for hcp-RuCo@C and hcp-Ru@C were determined to be 4.04 and 4.49 eV, respectively. The reduced WF value in hcp-RuCo@C suggested that alloying Co with Ru facilitated electron transfer from the catalyst's interior to its surface, accelerating electron exchange with reactants and thus expediting the reaction dynamics [32]. Moreover, the valence band maximum (VBM) values for hcp-RuCo@C and hcp-Ru@C were measured at 3.31 eV and 3.42 eV, respectively. It was evident that alloying Co with Ru shifted the valence band of hcp-RuCo@C closer to the Fermi level (E_f), indicating improved electrical conductivity [32,33].

3.2. Electrocatalytic performance in alkaline media

The electrocatalytic peculiarity of the catalysts were evaluated via the rotating disk electrode (RDE) technique in H_2-saturated 0.1 M KOH electrolyte, following reversible hydrogen electrode (RHE) calibration (Fig. S3). Through systematic experiments varying temperature and Ru content, we ascertained that hcp-RuCo@C exhibited superior hydrogen oxidation reaction (HOR) activity at an optimal temperature of 500 °C and a Ru content of 4.68 wt.% (Figs. S4-5). Subsequently, we qualitatively assessed the HOR activities of hcp-RuCo@C, hcp-Ru@C, Co@C and commercial Pt/C by examining the current responses. Fig. 3a demonstrated that hcp-RuCo@C displayed the highest anodic current density across the potential range region, outperforming both hcp-Ru@C and commercial Pt/C. A control experiment (Fig. S6) conducted in N_2-saturated electrolyte showcased inappreciable current–voltage feature, validating that the anodic current chiefly rooted in H_2 oxidation rather than other species. Moreover, we assessed the HOR polarization curves (Fig. 3b) of hcp-RuCo@C as a function of rotating speed to analyze the catalytic process, revealing that the limiting current density grew with the mounting rotational rate, certifying an H_2 mass-transfer-controlled process [34]. The Koutecky-Levich plot at 50 mV (inset of Fig. 3b) showed a linear relationship between the reciprocal of the current density and the square root of rotation speed, yielding a slope of 4.51 $cm^2\ mA^{-1}\ s^{-1/2}$, approach to the theoretical value (4.87 $cm^2\ mA^{-1}\ s^{-1/2}$) for a two-electron transfer HOR process [35,36].

To elucidate the HOR catalytic mechanism, Tafel slopes were derived from the relationship between the kinetic current density (j_k) and overpotential for the studied catalysts (Fig. 3c). The asymmetry behavior in Tafel plot elucidated that hcp-RuCo@C operated according

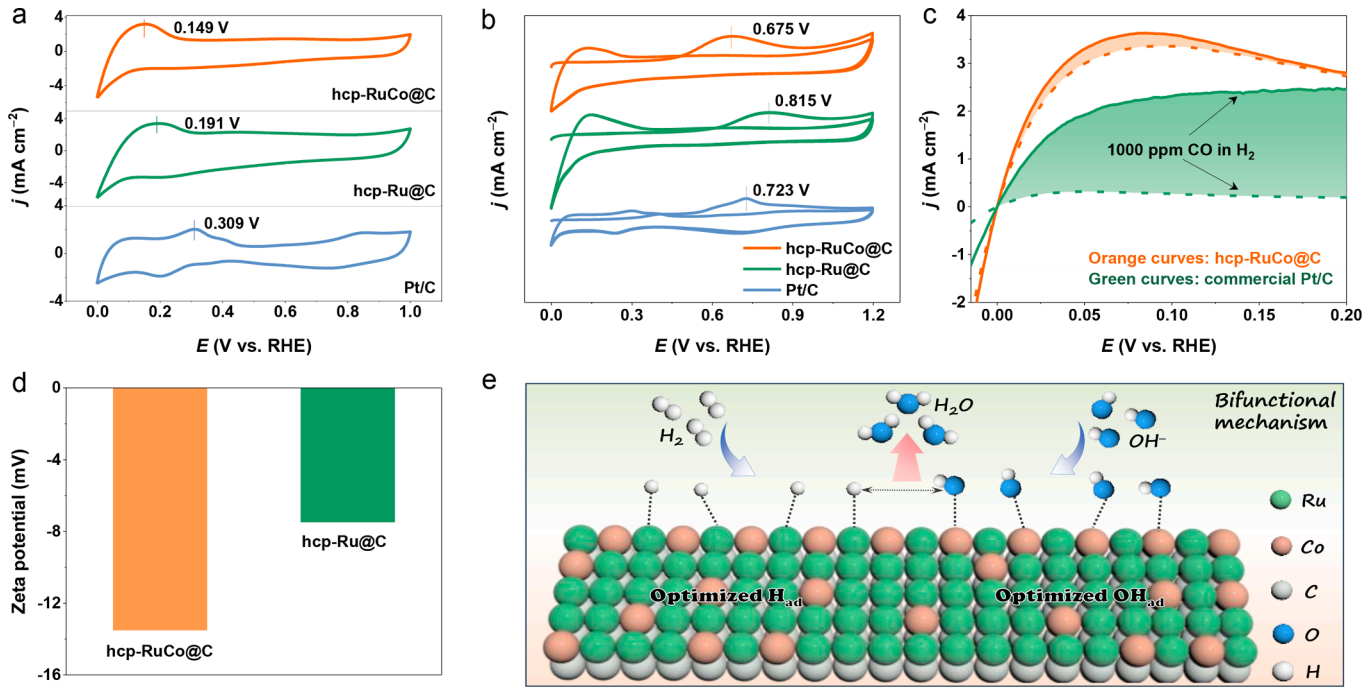

Fig. 4. (a) CV curves of hcp-RuCo@C, hcp-Ru@C and Pt/C. (b) CO stripping curves of hcp-RuCo@C, hcp-Ru@C and Pt/C. (c) HOR polarization curves of hcp-RuCo@C and Pt/C in 1000 ppm CO/H_2-saturated 0.1 M KOH. (d) Zeta potential of hcp-RuCo@C and hcp-Ru@C. (e) Schematic illustration of HOR catalysis on hcp-RuCo@C.

to the Heyrovsky-Volmer mechanism, with the Volmer step was identified as the rate-determining step (RDS). As plotted in Fig. 3d, the j_0 of samples were acquired from the micro-polarization region (−5 to 5 mV). The j_0 of hcp-RuCo@C (3.73 mA cm^{-2}) exceeded those of hcp-Ru@C (2.67 mA cm^{-2}) and commercial Pt/C (1.83 mA cm^{-2}), indicating the favorable inherent HOR activity of hcp-RuCo@C (Fig. 3e). Additionally, the j_k value at 50 mV was obtained from Koutecky-Levich equation. hcp-RuCo@C possessed a geometric j_k of 40.34 mA cm^{-2}, representing 2.2- and 5.9-fold increases compared to hcp-Ru@C (18.15 mA cm^{-2}) and commercial Pt/C (6.74 mA cm^{-2}), respectively. Furthermore, the j_k value of hcp-RuCo@C was normalized by the specific Ru loading to obtain the mass activity (MA) at 50 mV, The MA value of hcp-RuCo@C yielded to be 2.8 mA μg_{Ru}^{-1}, substantially overmatching that of most documented Ru-based catalysts (Fig. 3f).

Long-term stability was evaluated by operating 1000 CV cycles and chronoamperometry (*j*-t) measurements in an H_2-saturated 0.1 M KOH electrolyte. Fig. 3g exhibited that the HOR polarization curves of hcp-RuCo@C before and after 1000 cycles overlapped well, and the limiting current density showed only a slight recession even after 5000 cycles (Fig. S7). In addition, hcp-RuCo@C maintained HOR reactivity throughout the test without significant degradation, contrasting sharply with the substantial decline observed in commercial Pt/C (Fig. 3h). Simultaneously, the morphology of hcp-RuCo@C after the HOR test remained unchanged (insert in Fig. 3h). These results collectively verified the outstanding electrochemical stability of hcp-RuCo@C.

3.3. Catalytic mechanism analysis

Indeed, the alkaline hydrogen oxidation reaction (HOR) activity is intricately tied to the binding energies of intermediates, H_{ad} (HBE) and OH_{ad} (OHBE), crucial in the rate-determining Volmer step [37,38]. To gain a deeper understanding of the catalytic process, we meticulously examined the electrochemical desorption profiles associated with hydrogen underpotential deposition (H_{UPD}) and CO-stripping curves for investigated catalysts. These are persuasive electrochemical methods for probing the adsorption behavior of H_{ad} and OH_{ad} on platinum group metals (PGM)-based catalysts [39,40]. The shifting of H_{UPD} peak towards lower potentials in cyclic voltammetry (CV) signified a weaker binding of hydrogen [41]. As observed in Fig. 4a, the H_{UPD} peak of hcp-RuCo@C was situated at 0.149 V vs. RHE, more negative than those of hcp-Ru@C (0.191 V) and Pt/C (0.309 V), indicating a relatively weakened HBE for hcp-RuCo@C, thereby accelerating the Volmer step according to the bifunctional mechanism [42]. Since the anodic current of CO oxidation can only be initiated by reactive OH_{ad}, CO-stripping curves were employed to monitor OH_{ad} [37]. The CO oxidation peak (Fig. 4b) of hcp-RuCo@C appeared at 0.675 V, which shifted negatively compared to hcp-Ru@C (0.815 V) and Pt/C (0.723 V). After alloying Co with Ru, hcp-RuCo@C exhibited a stronger OHBE and better HOR properties than hcp-Ru@C, underscoring the beneficial role of Co. This enhancement is primarily attributed to the relatively oxophilic nature of Co, which facilitated the capture of hydroxide species and reduced the hydrogen adsorption species on catalyst surface. The appropriate OHBE of hcp-RuCo@C modulated the alkaline HOR process and prevented the poisoning of active sites, ameliorating the CO tolerance [40]. As projected, the HOR current of hcp-RuCo@C showed little change in an H_2 atmosphere containing 1000 ppm CO, corroborating the efficient oxidation of CO by OH_{ad} to mitigate catalyst poisoning (Fig. 4c). In stark contrast, the LSV polarization curve of commercial Pt/C exhibited a significant decline from its initial state, indicating that the active sites on its catalytic surface were predominantly occupied or poisoned by CO, which obstructed the hydrogen adsorption/dissociation sites [43]. Furthermore, the zeta potential measurements also confirmed that hcp-RuCo@C demonstrated the strongest hydroxyl adsorption (Fig. 4d and Fig. S8). Consequently, the diminished HBE and augmented OHBE on hcp-RuCo@C electrocatalyst surface achieved an optimal balance between H_{ad} and OH_{ad}, leading to exemplary HOR performance (Fig. 4e).

Taken together, the enhanced electrocatalytic performance of hcp-RuCo@C stemmed from several contributing factors. Firstly, the unique hollow porous carbon support provided ample space for anchoring nanoalloy particles, ensuring their uniform distribution within the pores of the porous support, thereby effectively preventing particle aggregation. Secondly, the hollow spherical structure of hcp-

RuCo@C possessed a larger specific surface area, which was beneficial for exposing more active sites and providing a high contact area with H_2 and electrolytes, thus accelerating the effective electrons/mass transfer. Thirdly, the RuCo alloying-induced *d-d* electronic interactions optimized both HBE and OHBE, significantly expediting the pivotal Volmer step and fortifying the alkaline HOR performance.

4. Conclusion

In summary, we have successfully engineered a high-performance hcp-RuCo@C electrocatalysts with an unconventional strong *d–d* orbital hybridization. Characterization techniques confirmed the large specific surface area and abundant pore structure of hcp-RuCo@C, facilitating efficient reactant access to active sites and enhancing catalytic efficiency. As anticipated, the resulting hcp-RuCo@C performed vastly decent HOR mass activity and exchange current density relative to pure hcp-Ru@C and commercial Pt/C respectively. Furthermore, hcp-RuCo@C was commendable for its virtue to continuously catalyze the H_2 oxidation without evident degradation and possessed superb CO tolerance. Experimental results revealed that Ru-Co alloying-induced the strong *d-d* electron interaction optimized the adsorption of both hydrogen and hydroxyl species, thereby accelerating the rate-determining Volmer step. This work elucidates the paramount role of *d–d* orbital hybridization in optimizing electrocatalytic activity and offers valuable insights for designing innovative catalysts with conspicuous HOR properties.

CRediT authorship contribution statement

Yi Liu: Writing – original draft, Conceptualization. **Lianrui Cheng:** Methodology. **Shuqing Zhou:** Investigation. **Chenggong Niu:** Data curation. **Tayirjan Taylor Isimjan:** Writing – review & editing. **Xiulin Yang:** Writing – review & editing, Supervision, Funding acquisition.

Declaration of competing interest

The authors declare that they have no known competing financial interests or personal relationships that could have appeared to influence the work reported in this paper.

Data availability

Data will be made available on request.

Acknowledgements

This work has been supported by the National Natural Science Foundation of China (no. 52363028, 21965005), Natural Science Foundation of Guangxi Province (2021GXNSFAA076001, 2018GXNSFAA294077), Guangxi Technology Base and Talent Subject (GUIKE AD23023004, GUIKE AD20297039). Innovation Project of Guangxi Graduate Education (YCSW2024228).

Appendix A. Supplementary data

Supplementary data to this article can be found online at https://doi.org/10.1016/j.jcis.2024.08.136.

References

[1] Y. Fang, C. Wei, Z. Bian, X. Yin, B. Liu, Z. Liu, P. Chi, J. Xiao, W. Song, S. Niu, C. Tang, J. Liu, X. Ge, T. Xu, G. Wang, Unveiling the nature of Pt-induced anti-deactivation of Ru for alkaline hydrogen oxidation reaction, Nat. Commun. 15 (2024) 1614.
[2] X. Tian, R. Ren, F. Wei, J. Pei, Z. Zhuang, L. Zhuang, W. Sheng, Metal-support interaction boosts the stability of Ni-based electrocatalysts for alkaline hydrogen oxidation, Nat. Commun. 15 (2024) 76.
[3] Y. Zhao, X. Wang, Z. Li, P. Zhao, C. Tao, G. Cheng, W. Luo, Enhanced catalytic activity of Ru through N modification toward alkaline hydrogen electrocatalysis, Chin. Chem. Lett. 33 (2022) 1065–1069.
[4] B. Zhang, X. Qiu, T. Chen, C. Huang, X. Yue, S. Huang, Construction of Heterostructure between $Ni_{17}W_3$ and WO_2 to Boost the Hydrogen Oxidation Reaction in Alkaline Medium, ACS Appl. Mater. Interfaces 16 (2024) 3270–3278.
[5] X.Q. Mu, S.L. Liu, M.Y. Zhang, Z.C. Zhuang, D. Chen, Y.R. Liao, H.Y. Zhao, S.C. Mu, D.S. Wang, Z.H. Dai, Symmetry-Broken Ru Nanoparticles with Parasitic Ru-Co Dual-Single Atoms Overcome the Volmer Step of Alkaline Hydrogen Oxidation, Angew. Chem. Int. Ed. 63 (2024) e202319618.
[6] W. Luo, P. Han, X. Yang, L. Wu, H. Jia, Revealing the Role of Bridging Oxygen in Carbon Shell Coated Ni Interface for Enhanced Alkaline Hydrogen Oxidation Reaction, Chem. Sci. 15 (2024) 5633–5641.
[7] C. Yang, J. Yue, G. Wang, W. Luo, Activating and Identifying the Active Site of RuS_2 for Alkaline Hydrogen Oxidation Electrocatalysis, Angew. Chem. Int. Ed. 63 (2024) e202401453.
[8] J. Gao, W. Yu, J. Liu, L. Qin, H. Cheng, X. Cui, L. Jiang, Regulation of hydrogen binding energy via oxygen vacancy enables an efficient trifunctional Rh-Rh_2O_3 electrocatalyst for fuel cells and water splitting, J. Colloid Interface Sci. 664 (2024) 766–778.
[9] X. Zhang, Z. Li, X. Sun, L. Wei, H. Niu, S. Chen, Q. Chen, C. Wang, F. Zheng, Regulating the Surface Electronic Structure of RuNi Alloys for Boosting Alkaline Hydrogen Oxidation Electrocatalysis, ACS Mater. Lett. 4 (2022) 2097–2105.
[10] M. Ma, G. Li, W. Yan, Z. Wu, Z. Zheng, X. Zhang, Q. Wang, G. Du, D. Liu, Z. Xie, Q. Kuang, L. Zheng, Single-Atom Molybdenum Engineered Platinum Nanocatalyst for Boosted Alkaline Hydrogen Oxidation, Adv. Energy Mater. 12 (2022) 2103336.
[11] C. Huang, M. Feng, Y. Peng, B. Zhang, J. Huang, X. Yue, S. Huang, In Situ Construction of Ni/$Ni_{0.2}Mo_{0.8}N$ Heterostructure to Enhance the Alkaline Hydrogen Oxidation Reaction by Balancing the Binding of Intermediates, Adv. Funct. Mater. 33 (2023) 2300593.
[12] Y. Liu, L. Cheng, Y. Huang, Y. Yang, X. Rao, S. Zhou, T. Taylor Isimjan, X. Yang, Electronic Modulation and Mechanistic Study of Ru-Decorated Porous Cu-Rich Cuprous Oxide for Robust Alkaline Hydrogen Oxidation and Evolution Reactions, ChemSusChem 16 (2023) e202202113.
[13] S. Wang, L. Fu, H. Huang, M. Fu, J. Cai, Z. Lyu, Q. Wang, Q. Kuang, Z. Xie, S. Xie, Local Oxidation Induced Amorphization of 1.5-nm-Thick Pt–Ru Nanowires Enables Superactive and CO-Tolerant Hydrogen Oxidation in Alkaline Media, Adv. Funct. Mater. 33 (2023) 2304125.
[14] X. Mu, S. Liu, L. Chen, S. Mu, Alkaline Hydrogen Oxidation Reaction Catalysts: Insight into Catalytic Mechanisms, Classification, Activity Regulation and Challenges, Small Struct. 4 (2023) 2200281.
[15] L. Su, X. Fan, Y. Jin, H. Cong, W. Luo, Hydroxyl-Binding Energy-Induced Kinetic Gap Narrowing between Acidic and Alkaline Hydrogen Oxidation Reaction on Intermetallic Ru_3Sn_7 Catalyst, Small 19 (2023) e2207603.
[16] G. Yang, Y. Yang, H. Qu, Y. Wang, C. Ru, H. Wu, Y. Han, J. Zhu, M. Xiao, C. Liu, W. Xing, Engineering Ru–RuO_2 interface with regulated hydroxyl adsorption towards efficient and CO-tolerant hydrogen oxidation reaction, Mater. Today Phys. 40 (2024) 101312.
[17] S. He, Y. Tu, J. Zhang, L. Zhang, J. Ke, L. Wang, L. Du, Z. Cui, H. Song, Ammonia-Induced FCC Ru Nanocrystals for Efficient Alkaline Hydrogen Electrocatalysis, Small 20 (2023) 2308053.
[18] X. Zhang, L. Xia, G. Zhao, B. Zhang, Y. Chen, J. Chen, M. Gao, Y. Jiang, Y. Liu, H. Pan, W. Sun, Fast and Durable Alkaline Hydrogen Oxidation Reaction at the Electron-Deficient Ruthenium-Ruthenium Oxide Interface, Adv. Mater. 35 (2023) 2208821.
[19] J. Park, H. Kim, S. Kim, S.Y. Yi, H. Min, D. Choi, S. Lee, J. Kim, J. Lee, Boosting Alkaline Hydrogen Oxidation Activity of Ru Single-Atom Through Promoting Hydroxyl Adsorption on Ru/WC_{1-x} Interfaces, Adv. Mater. 36 (2023) 2308899.
[20] J. Zhang, X. Fan, S. Wang, M. Cao, L. Bu, Y. Xu, H. Lin, X. Huang, Surface Engineered Ru_2Ni Multilayer Nanosheets for Hydrogen Oxidation Catalysis, CCS Chem. 5 (2022) 1931–1941.
[21] J.-T. Ren, L. Chen, H.-Y. Wang, Z.-Y. Yuan, Non-precious metal high-entropy alloy with d-d electron interaction for efficient and robust hydrogen oxidation reaction in alkaline media, Inorg. Chem. Front. 11 (2024) 2029–2038.
[22] M. Guo, M. Xu, Y. Qu, C. Hu, P. Yan, T.T. Isimjan, X. Yang, Electronic/mass transport increased hollow porous Cu_3P/MoP nanospheres with strong electronic interaction for promoting oxygen reduction in Zn-air batteries, Appl. Catal. B Environ. 297 (2021) 120415.
[23] Y. Liu, L. Cheng, S. Zhou, Y. Yang, C. Niu, T. Taylor Isimjan, B. Wang, X. Yang, Revealing interfacial charge redistribution of homologous Ru-RuS_2 heterostructure toward robust hydrogen oxidation reaction, J. Energy Chem. 94 (2024) 332–339.
[24] D. Zhao, K. Sun, W.C. Cheong, L. Zheng, C. Zhang, S. Liu, X. Cao, K. Wu, Y. Pan, Z. Zhuang, B. Hu, D. Wang, Q. Peng, C. Chen, Y. Li, Synergistically Interactive Pyridinic-N-MoP Sites: Identified Active Centers for Enhanced Hydrogen Evolution in Alkaline Solution, Angew. Chem. Int. Ed. 59 (2020) 8982–8990.
[25] Y. Yang, L. Shi, Q. Liang, Y. Liu, J. Dong, T.T. Isimjan, B. Wang, X. Yang, Uleashing efficient and CO-resilient alkaline hydrogen oxidation of Pd_3P through phosphorus vacancy defect engineering, Chin. J. Catal. 56 (2024) 176–187.
[26] W. Li, Y. Zhao, Y. Liu, M. Sun, G.I.N. Waterhouse, B. Huang, K. Zhang, T. Zhang, S. Lu, Exploiting Ru-Induced Lattice Strain in CoRu Nanoalloys for Robust Bifunctional Hydrogen Production, Angew. Chem. Int. Ed. 60 (2021) 3290–3298.
[27] X. Gao, B. Li, X. Sun, B. Wu, Y. Hu, Z. Ning, J. Li, N. Wang, Engineering heterostructure and crystallinity of Ru/RuS_2 nanoparticle composited with N-doped graphene as electrocatalysts for alkaline hydrogen evolution, Chin. Chem. Lett. 32 (2021) 3591–3595.

[28] J. Wu, Y. Zhou, H. Nie, K. Wei, H. Huang, F. Liao, Y. Liu, M. Shao, Z. Kang, Carbon dots regulate the interface electron transfer and catalytic kinetics of Pt-based alloys catalyst for highly efficient hydrogen oxidation, J. Energy Chem. 66 (2022) 61–67.
[29] W. Li, D. Wang, Y. Zhang, L. Tao, T. Wang, Y. Zou, Y. Wang, R. Chen, S. Wang, Defect Engineering for Fuel-Cell Electrocatalysts, Adv. Mater. 32 (2020) 1907879.
[30] X. Zhao, X. Yu, S. Xin, S. Chen, C. Bao, W. Xu, J. Xue, B. Hui, J. Zhang, X. She, D. Yang, Enhanced oxygen reduction reaction for Zn-air battery at defective carbon fibers derived from seaweed polysaccharide, Appl. Catal. B Environ. 301 (2022) 120785.
[31] Y. Li, C. Yang, C. Ge, N. Yao, J. Yin, W. Jiang, H. Cong, G. Cheng, W. Luo, L. Zhuang, Electronic Modulation of Ru Nanosheet by d-d Orbital Coupling for Enhanced Hydrogen Oxidation Reaction in Alkaline Electrolytes, Small 18 (2022) 2202404.
[32] Z. Huang, M. Liao, S. Zhang, L. Wang, M. Gao, Z. Luo, T.T. Isimjan, B. Wang, X. Yang, Valence electronic engineering of superhydrophilic Dy-evoked Ni-MOF outperforming RuO_2 for highly efficient electrocatalytic oxygen evolution, J. Energy Chem. 90 (2024) 244–252.
[33] Y. Song, M. Sun, S. Zhang, X. Zhang, P. Yi, J. Liu, B. Huang, M. Huang, L. Zhang, Alleviating the Work Function of Vein-Like Co_xP by Cr Doping for Enhanced Seawater Electrolysis, Adv. Funct. Mater. 33 (2023) 2214081.
[34] J. Zhang, G. Ren, D. Li, Q. Kong, Z. Hu, Y. Xu, S. Wang, L. Wang, M. Cao, X. Huang, Interface engineering of snow-like Ru/RuO_2 nanosheets for boosting hydrogen electrocatalysis, Sci. Bull. 67 (2022) 2103–2111.
[35] D.Q. Liu, Z. Luo, B. Zhang, G. Zhao, W. Guo, J. Chen, M. Gao, Y. Liu, H. Pan, W. Sun, Tailoring Interfacial Charge Transfer of Epitaxially Grown Ir Clusters for Boosting Hydrogen Oxidation Reaction, Adv. Funct. Mater. 13 (2022) 2202913.
[36] X. Ke, F. Zhou, Y. Chen, M. Zhao, Y. Yang, H. Jin, Y. Dong, C. Zou, X.A. Chen, L. Zhang, S. Wang, Modifying charge transfer between Rhodium and Ceria for boosted hydrogen oxidation reaction in alkaline electrolyte, J. Colloid Interface Sci. 650 (2023) 1842–1850.
[37] T. Tang, X. Liu, X. Luo, Z. Xue, H.R. Pan, J. Fu, Z.C. Yao, Z. Jiang, Z.H. Lyu, L. Zheng, D. Su, J.N. Zhang, L. Zhang, J.S. Hu, Unconventional Bilateral Compressive Strained Ni-Ir Interface Synergistically Accelerates Alkaline Hydrogen Oxidation, J. Am. Chem. Soc. 145 (2023) 13805–13815.
[38] W. Li, K. Liu, S. Feng, Y. Xiao, L. Zhang, J. Mao, Q. Liu, X. Liu, J. Luo, L. Han, Well-defined Ni_3N nanoparticles armored in hollow carbon nanotube shell for high-efficiency bifunctional hydrogen electrocatalysis, J. Colloid Interface Sci. 655 (2024) 726–735.
[39] Y. Dong, Z. Zhang, W. Yan, X. Hu, C. Zhan, Y. Xu, X. Huang, Pb-Modified Ultrathin RuCu Nanoflowers for Active, Stable, and CO-resistant Alkaline Electrocatalytic Hydrogen Oxidation, Angew. Chem. Int. Ed. 62 (2023) e202311722.
[40] L. Wang, Z. Xu, C.-H. Kuo, J. Peng, F. Hu, L. Li, H.-Y. Chen, J. Wang, S. Peng, Stabilizing Low-Valence Single Atoms by Constructing Metalloid Tungsten Carbide Supports for Efficient Hydrogen Oxidation and Evolution, Angew. Chem. Int. Ed. 62 (2023) e202311937.
[41] M. Wang, C. Tang, S. Geng, C. Zhan, L. Wang, W.-H. Huang, C.-W. Pao, Z. Hu, Y. Li, X. Huang, L. Bu, Compressive Strain in Platinum–Iridium–Nickel Zigzag-Like Nanowire Boosts Hydrogen Catalysis, Small 20 (2023) 2310036.
[42] M. Wang, L. Yang, Z. Qiu, P. Lu, H. Sun, J. Chen, J. Sun, C.-P. Li, Synergistic Ru/CeO_2 heterostructure for alkaline hydrogen oxidation with high activity and CO tolerance, Int. J. Hydrogen Energy 48 (2023) 34355–34362.
[43] J. Cai, X. Zhang, Z. Lyu, H. Huang, S. Wang, L. Fu, Q. Wang, X.-F. Yu, Z. Xie, S. Xie, Host-Guest Ensemble Effect on Dual-Pt atom-on-Rh Nanosheets Enables High-Efficiency and Anti-CO Alkaline Hydrogen Oxidation, ACS Catal. 13 (2023) 6974–6982.